Supplement to: Diurnal cycles of deep convective processes: Biases of ERA5 and DYAMOND km-scale models revealed by satellite observations of frozen water path and precipitation

Lara Leko[1,*], Gunnar Behrens[1,*], Nils Müller[1,a], Adrià Amell[1], Axel Lauer[2], and Patrick Eriksson[1]

[1]Chalmers University of Technology, Gothenburg, Sweden
[2]Deutsches Zentrum für Luft- und Raumfahrt (DLR), Institut für Physik der Atmosphäre, Oberpfaffenhofen, Germany
[*]These authors contributed equally to this work.
[a]now at: Alfred-Wegener-Institut, Helmholtz-Zentrum für Polar- und Meeresforschung (AWI), Bremerhaven, Germany

1 DYAMOND

2 Supplementary Figures

Models	FWP Variables	precip variables	hor. res. Δx	temp. res. Δt	CP	OC	FWP preprocess.	precip preprocess.
GEM	clivi [a], qgvi [b], qsvi [c]	-	∼5	60	None	No	adding together snow, graupel and ice water paths	-
GEOS	clivi, qgvi, qsvi	pr [d]	∼3	15	Full	No	adding snow, graupel and ice water paths	mass flux converted to mm/h
GFDL	clivi, qgvi, qsvi	-	∼3	15	Shallow	No	adding snow, graupel and ice water paths	-
GRIST	clivi, qgvi, qsvi	-	∼5	15	None	Yes	adding snow, graupel and ice water paths	-
GSAM	clivi, qgvi, qsvi	pracc [e]	∼4	15	None	No	adding snow, graupel and ice water paths	differentiated and converted mass flux to mm/h
ICON	clivi, qgvi, qsvi	pr	∼5	15	None	Yes	adding snow, graupel and ice water paths	mass flux converted to mm/h
IFS	clivi, qsvi	pracc	∼4	60	Shallow	Yes	adding snow and ice water paths, graupel is included in snow	differentiated and converted mass flux to mm/h
MPAS	clivi, qgvi, qsvi	-	∼3.75	15	Full	No	adding snow, graupel and ice water paths	converted to mm/h
ARPEGE	clivi, qgvi, qsvi	pr	∼2	15	None	No	adding snow, graupel and ice water paths	converted to mm/h
SHiELD	-	pr	∼2	15	Shallow	No	adding snow, graupel and ice water paths	mass flux converted to mm/h

[a] atmosphere mass content of ice
[b] atmosphere mass content of graupel
[c] atmosphere mass content of snow
[d] precipitation flux
[e] accumulated precipitation flux

Table S1. DYAMOND models from the winter project (Stevens et al., 2019), their spatial resolution at the Equator, temporal resolution, Convective Parametrisation (CP), Ocean Coupling (OC) and pre-processing for FWP and precipitation.

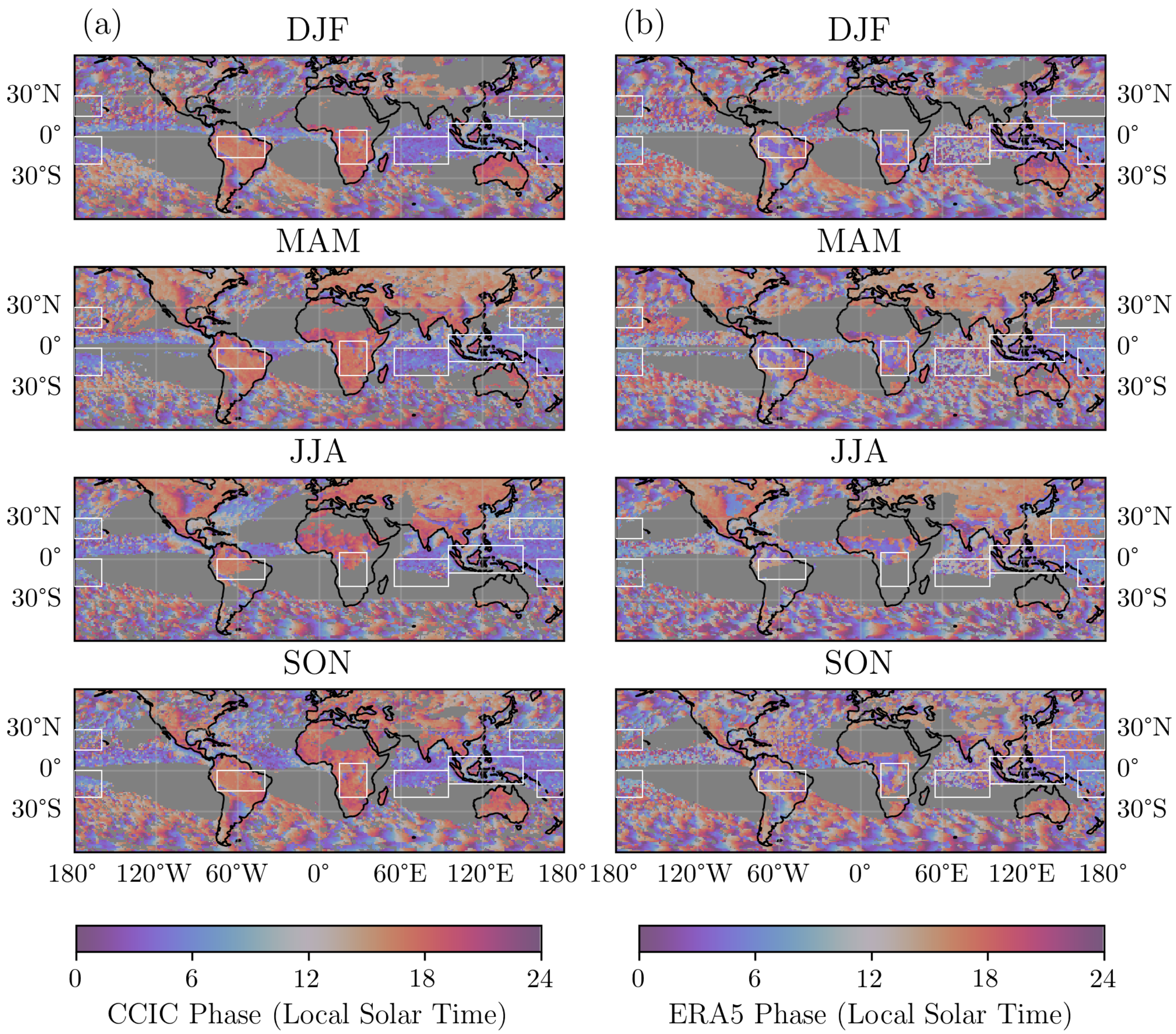

Figure S1. Latitude-Longitude maps of the diurnal peak time of FWP for the period 2018 to 2023 similar to Fig.2 but in absolute Local Solar Time for ERA5 for all seasons. The left column shows CCIC and the right column shows ERA5. Areas with a low FWP or low diurnal variability are masked. In addition the six tropical boxes for the regional analysis are indicated.

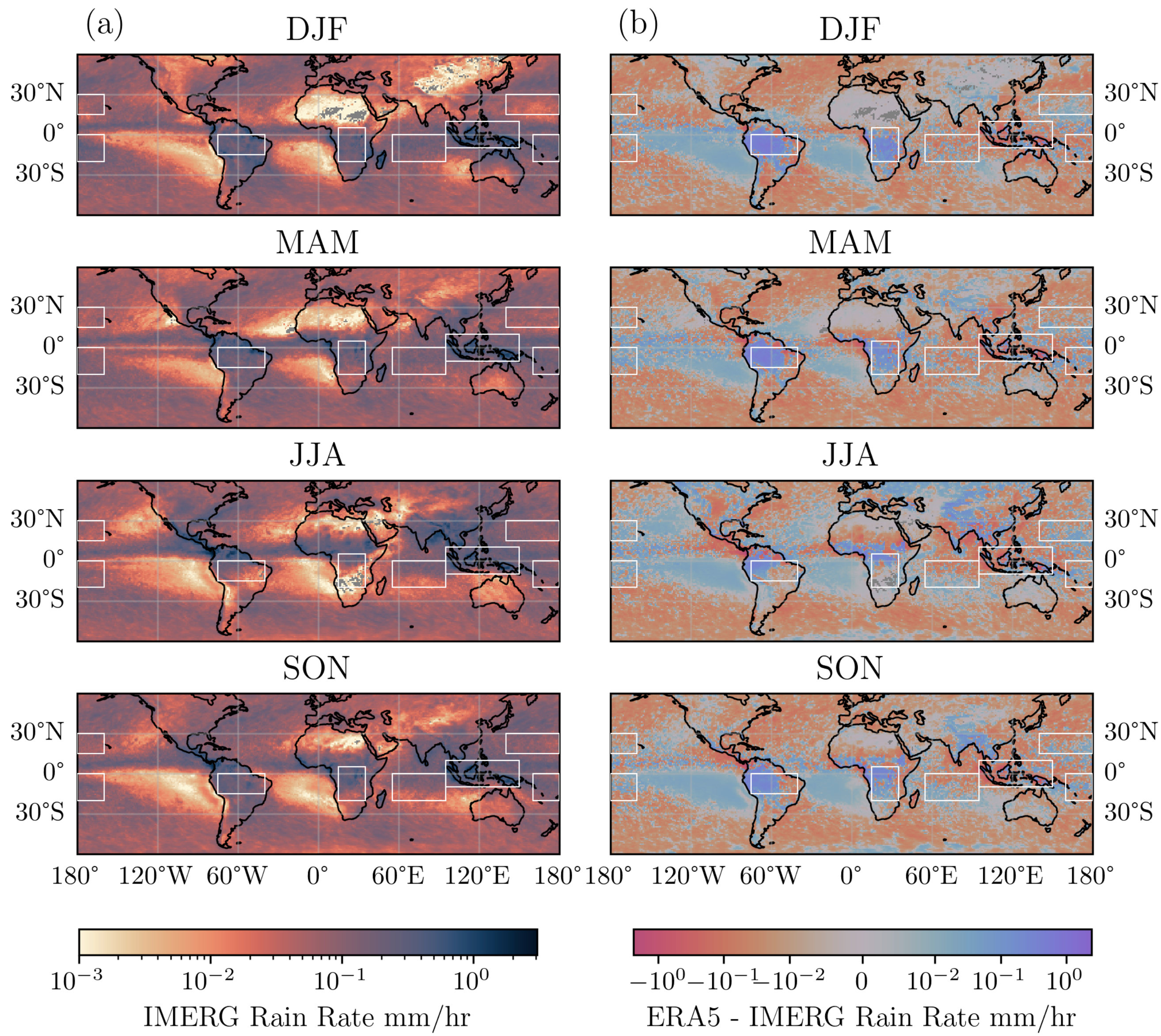

Figure S2. Latitude-Longitude maps of the diurnal amplitude of precip for the period 2018 to 2023 for all seasons. a) shows the diurnal amplitude of precip for IMERG, while b) depicts the difference of ERA5 and IMERG. We indicated again the edges of the six tropical boxes for the regional analysis similar to Fig. S1 of this supplement.

References

Stevens, B., Satoh, M., Auger, L., Biercamp, J., Bretherton, C. S., Chen, X., Düben, P., Judt, F., Khairoutdinov, M., Klocke, D., et al.: DYAMOND: the DYnamics of the Atmospheric general circulation Modeled On Non-hydrostatic Domains, Progress in Earth and Planetary Science, 6, 1–17, https://doi.org/https://doi.org/10.1186/s40645-019-0304-z, 2019.

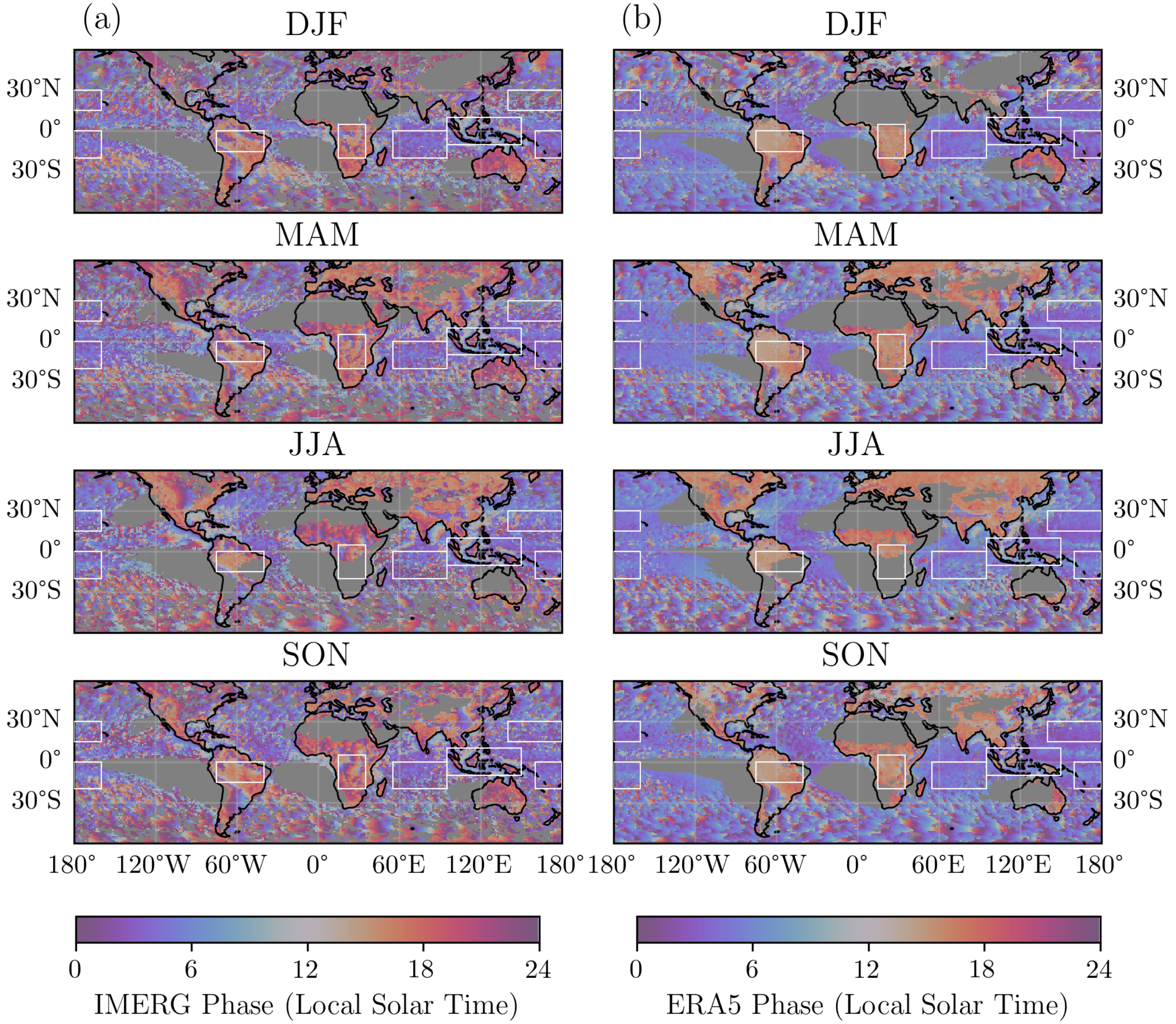

Figure S3. Latitude-Longitude maps of the diurnal peak time of precip for the period 2018 to 2023 for all seasons. The left column shows the diurnal peak time of precip for IMERG, while the right column depicts the diurnal peak time of ERA5 for all seasons. Areas with low precip or low diurnal variability of precip are masked. We indicated again the edges of the six tropical boxes for the regional analysis similar to Fig. S1 of this supplement.

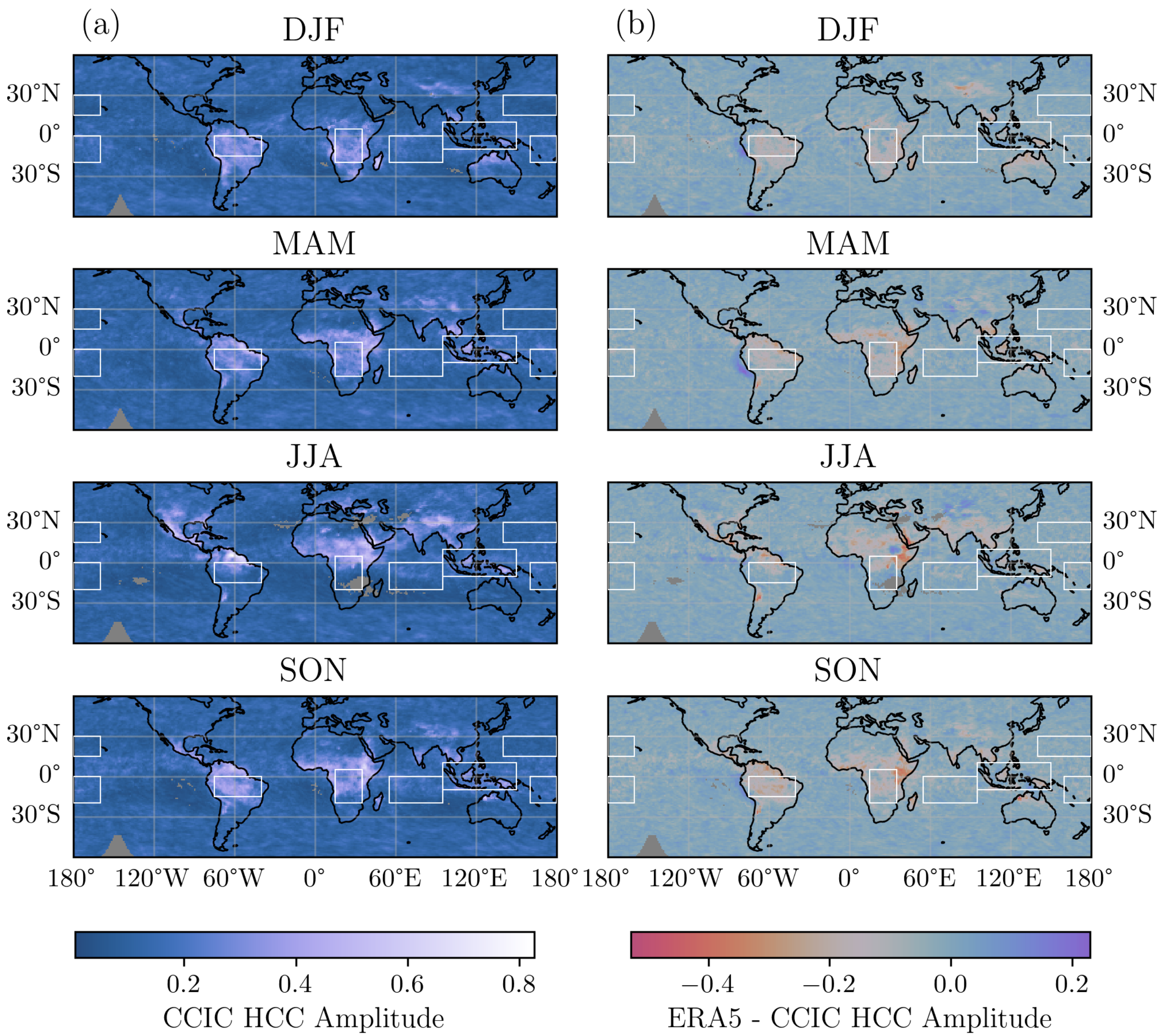

Figure S4. Latitude-Longitude maps of the diurnal amplitude of HCC for the year 2018 for all seasons. a) shows the diurnal amplitude of HCC of CCIC, while b) depcits the diurnal amplitude difference of HCC of ERA5 and CCIC. Areas with low HCC or low dirunal variability of HCC are masked. We indicated again the edges of the six tropical boxes for the regional analysis similar to Fig. S1 of this supplement.

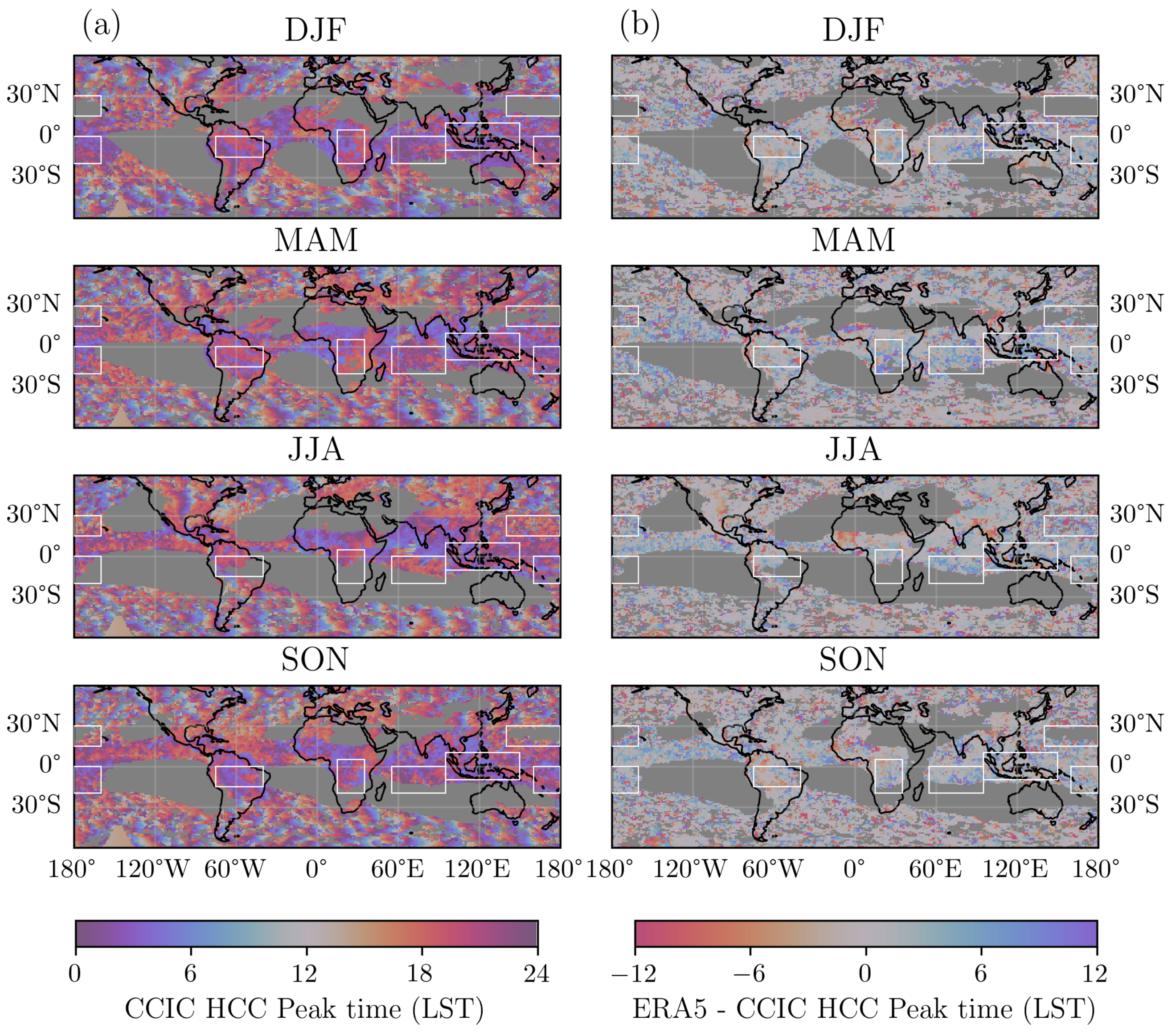

Figure S5. Latitude-Longitude maps of the diurnal peak time of HCC for the year 2018 for all seasons. The left column shows the diurnal peak time of CCIC, while the right column shows the difference between ERA5 and CCI. Areas with low HCC or low diurnal variability of HCC are masked. We indicated again the edges of the six tropical boxes for the regional analysis similar to Fig. S1 of this supplement.

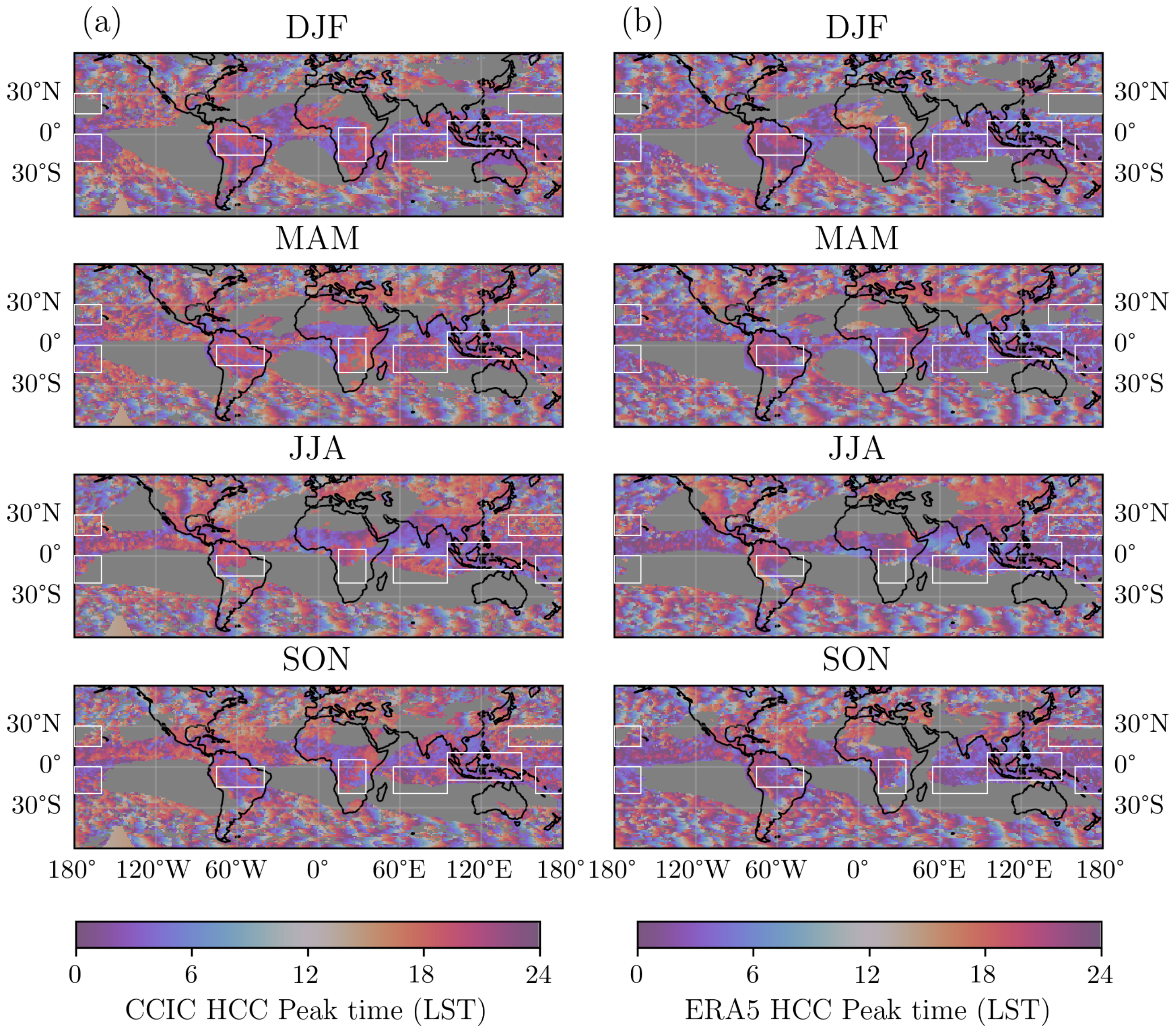

Figure S6. Similar to Fig. S5 of this supplement but with absolute peak time of diurnal HCC in LST for ERA5 for the year 2018.

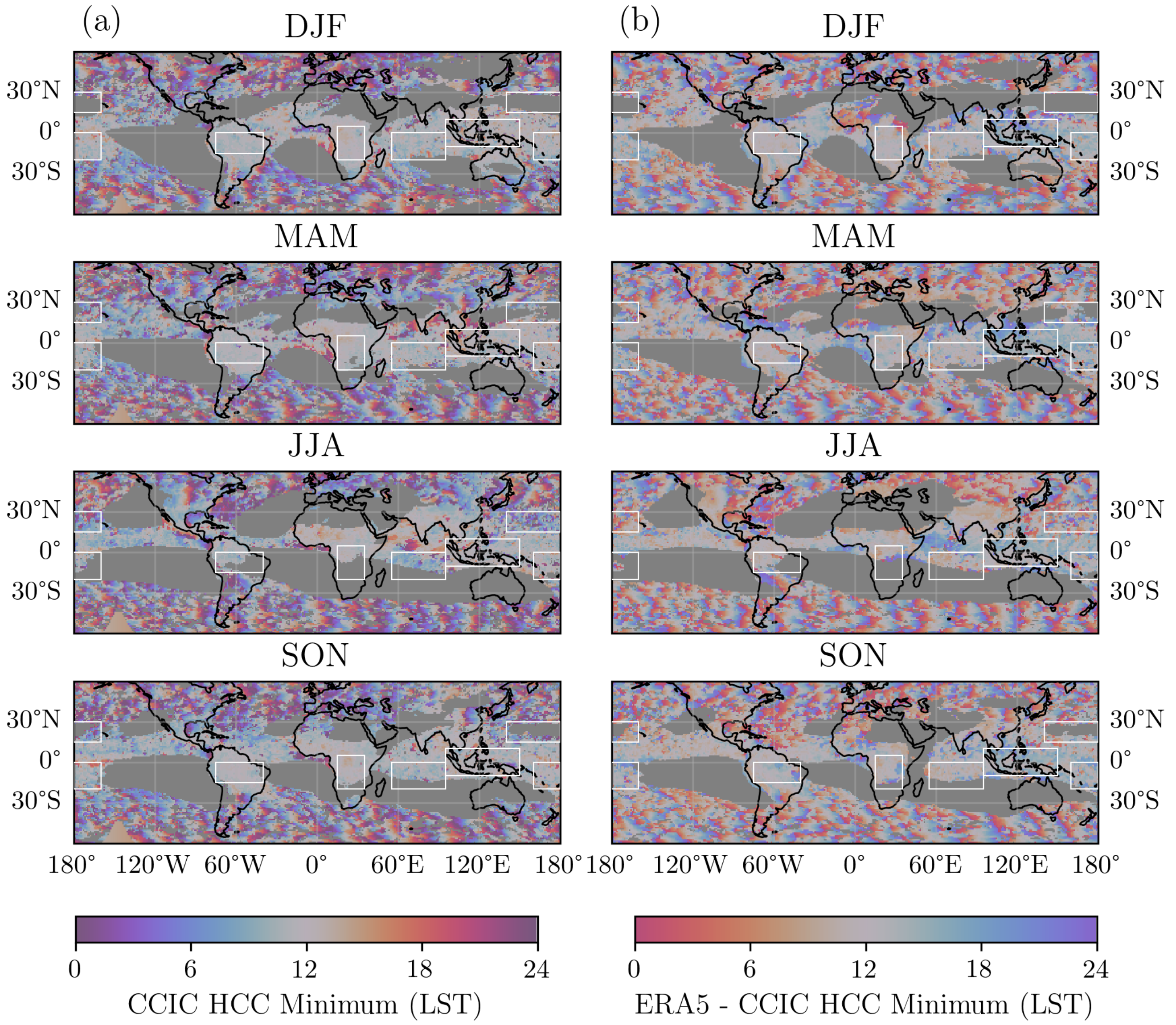

Figure S7. Similar to Fig. S5 of this supplement but with occurrence of the local minimum of HCC in LST for CCIC and the respective difference of ERA5 - CCIC for all seasons of the year 2018

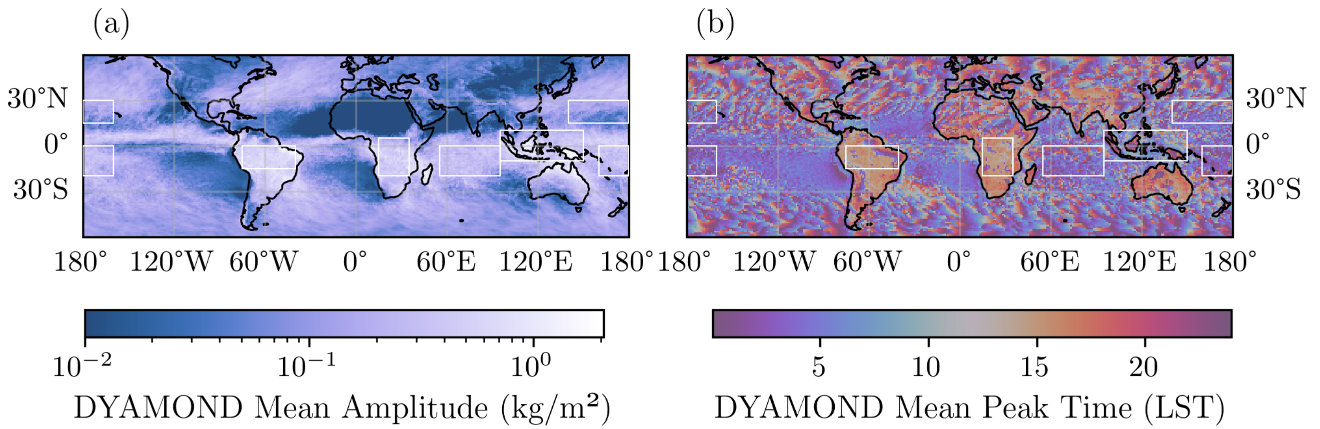

Figure S8. Multi-model mean of DYAMOND models in terms of their FWP diurnal amplitude (a) and peak time in LST (b) for February 2020.

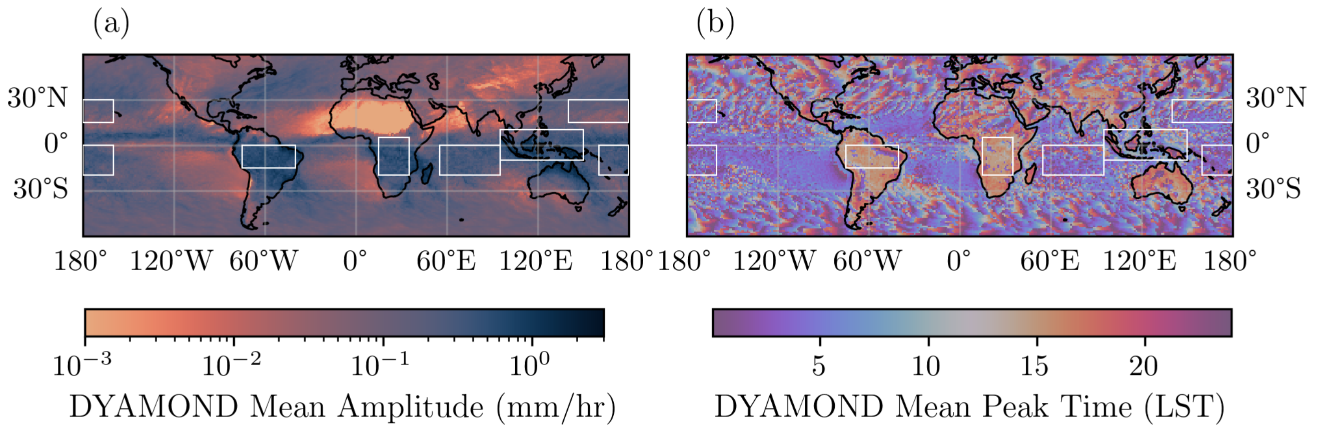

Figure S9. Multi-model mean of DYAMOND models in terms of their precipitation diurnal amplitude (a) and peak time in LST (b) for February 2020.

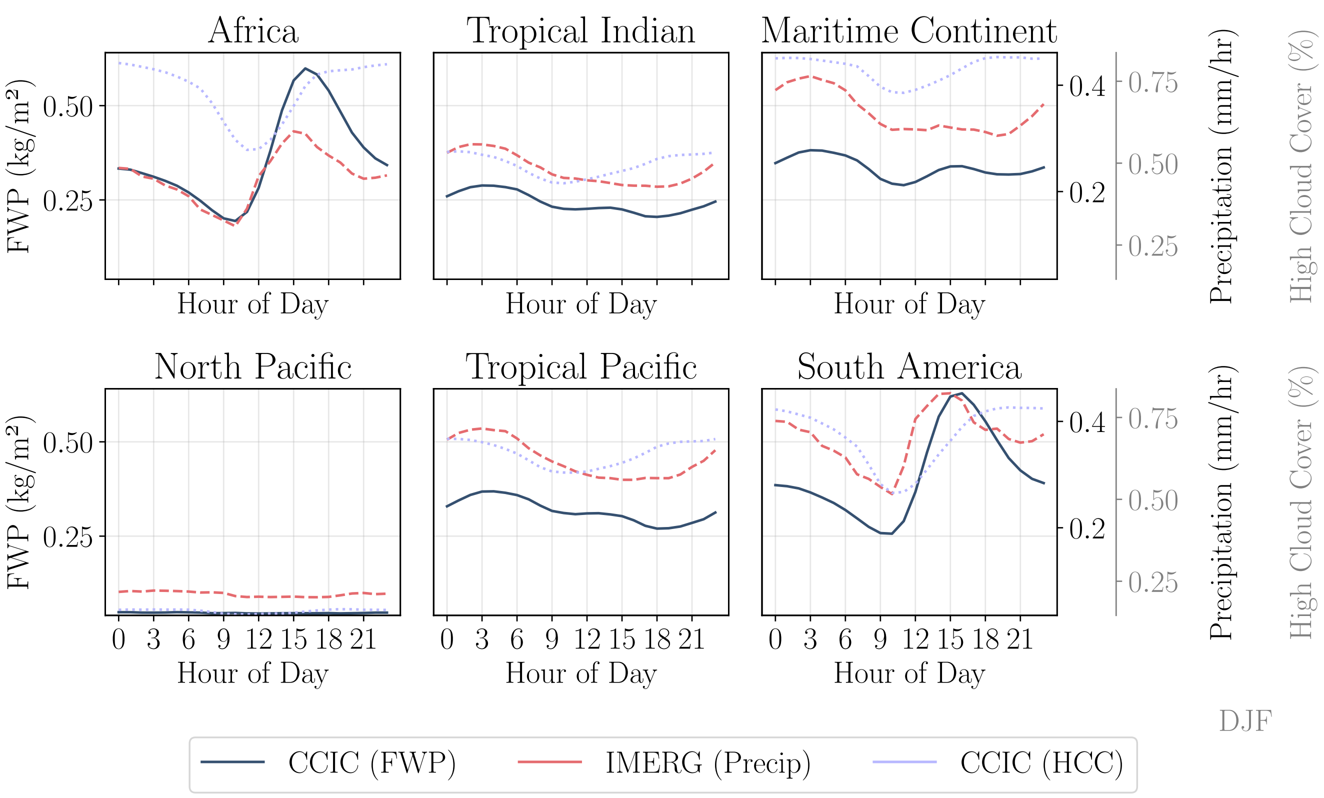

Figure S10. Composite of the satellite observed regionally averaged diurnal cycles during the winter months (DJF) of 2018/19 in the six tropical boxes. The blue solid curve in each panel indicates the averaged diurnal cycle of FWP in CCIC. The red dashed line indicates the diurnal cycle in precip of IMERG, while the dotted light purple curves depicts the average diurnal cycle of HCC in CCIC.

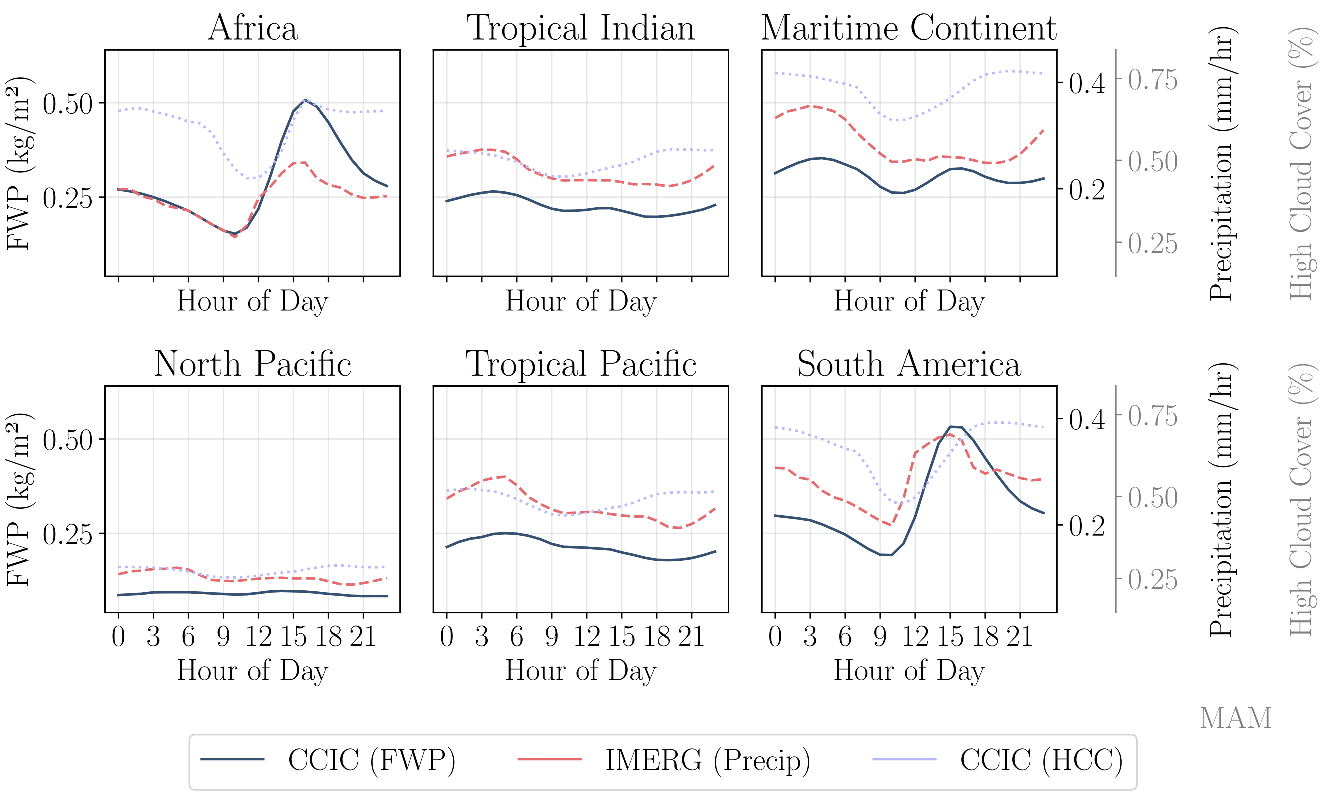

Figure S11. Similar to Fig. S10 but during spring (MAM) of the year 2018.

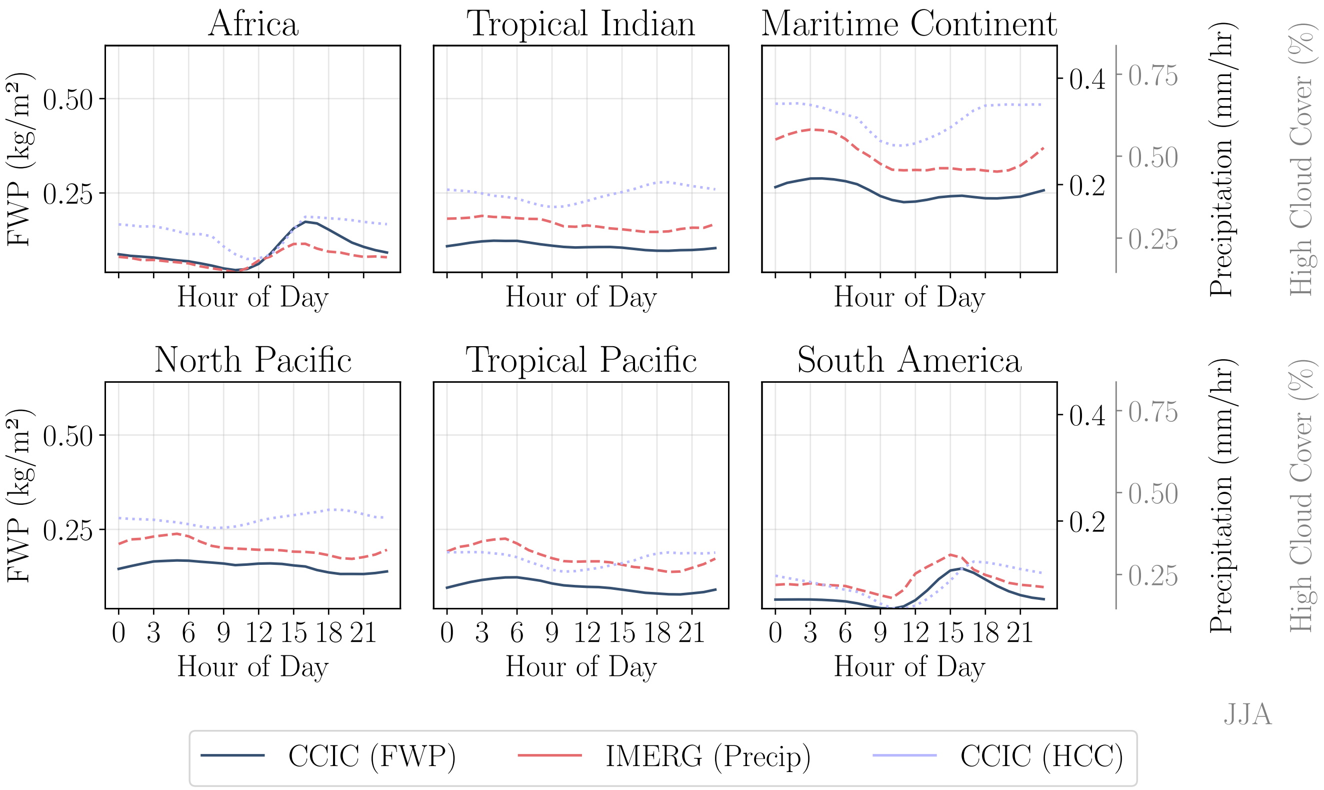

Figure S12. Similar to Fig. S10 but during summer (JJA) of the year 2018.

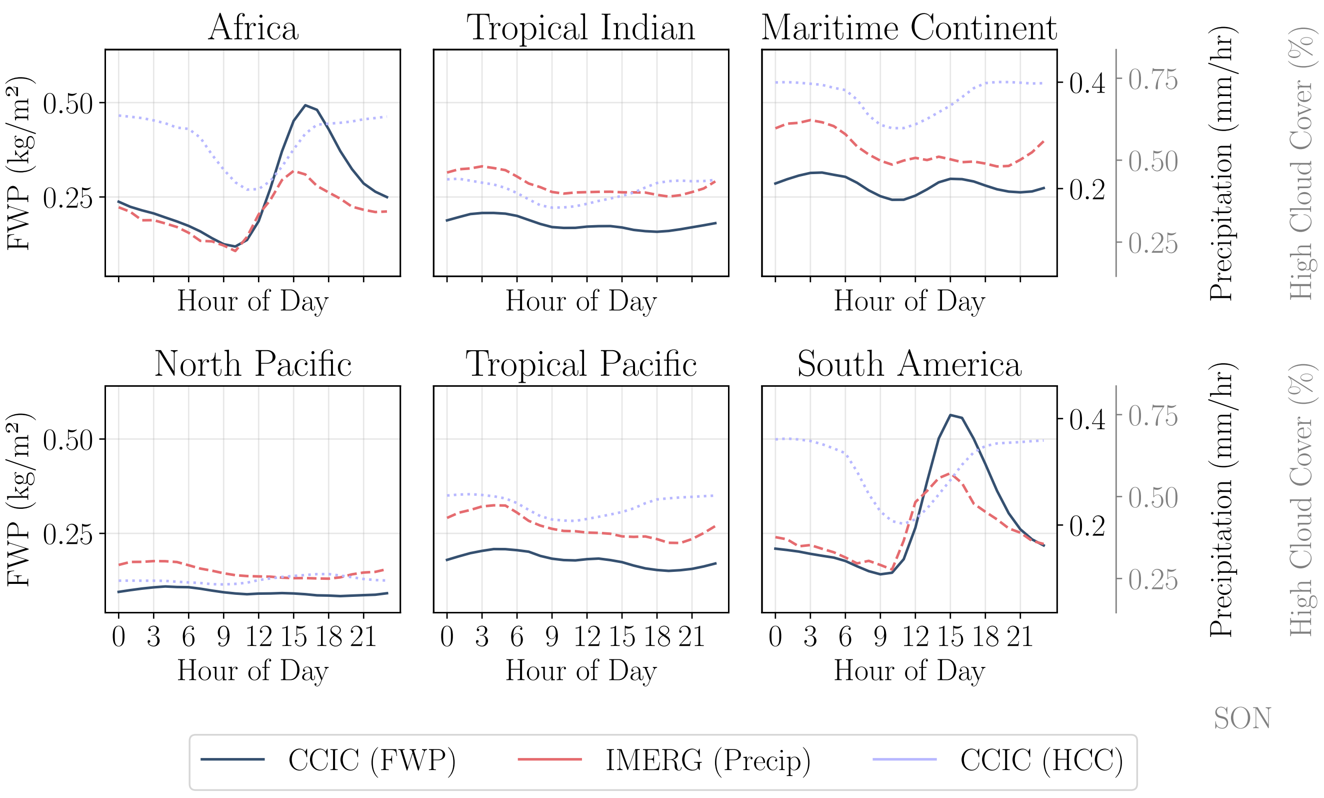

Figure S13. Similar to Fig. S10 but during fall (SON) of the year 2018.